

# Nanoscale Free-Carrier Profiling of Individual Semiconductor Nanowires by Infrared Near-Field Nanoscopy

J. M. Stiegler,<sup>†</sup> A. J. Huber,<sup>‡</sup> S. L. Diedenhofen,<sup>§</sup> J. Gómez Rivas,<sup>§</sup> R. E. Algra,<sup>||,⊥,¶</sup>  
E. P. A. M. Bakkers,<sup>¶</sup> and R. Hillenbrand<sup>\*,†,△</sup>

<sup>†</sup>CIC nanoGUNE Consolider, 20018 Donostia—San Sebastian Spain, <sup>‡</sup>Neaspec GmbH, 82152 Martinsried, Germany, <sup>§</sup>FOM Institute AMOLF, c/o Philips Research Laboratories, 5656 AE Eindhoven, The Netherlands, <sup>||</sup>Materials Innovation Institute, 2628 CD Delft, The Netherlands, <sup>⊥</sup>Institute for Molecules and Materials, Solid State Chemistry Department, Radboud University Nijmegen, 6525 ED Nijmegen, The Netherlands, <sup>¶</sup>Philips Research Laboratories, 5656 AE Eindhoven, The Netherlands, and <sup>△</sup>IKERBASQUE, Basque Foundation for Science, 48011 Bilbao, Spain

**ABSTRACT** We report quantitative, noninvasive and nanoscale-resolved mapping of the free-carrier distribution in InP nanowires with doping modulation along the axial and radial directions, by employing infrared near-field nanoscopy. Owing to the technique's capability of subsurface probing, we provide direct experimental evidence that dopants in interior nanowire shells effectively contribute to the local free-carrier concentration. The high sensitivity of s-SNOM also allows us to directly visualize nanoscale variations in the free-carrier concentration of wires as thin as 20 nm, which we attribute to local growth defects. Our results open interesting avenues for studying local conductivity in complex nanowire heterostructures, which could be further enhanced by near-field infrared nanotomography.

**KEYWORDS** Nanowires, doping, free-carrier profiling, infrared near-field microscopy, plasmons

Semiconductor nanowires bear enormous potential as building blocks for future nano(opto)electronic devices,<sup>1–6</sup> including lasers, transistors, and biosensors. A widely used method for fabricating semiconductor nanowires is the vapor–liquid–solid (VLS) growth. It allows the variation of diameter and length as well as the local chemical composition<sup>7</sup> and doping concentration<sup>8</sup> of the nanowires. The possibility to control the physical properties on an atomic level may open the door to completely new electronic structures and devices.<sup>9</sup> As the VLS wire-growth occurs at the interface between a metallic particle that acts as catalyst and the semiconductor nanowire, it is directed along the longitudinal axis of the wire. But also radial growth takes place with a much slower growth rate as it is not catalyzed by the metallic particle.<sup>10</sup> Existing segments of the nanowires thus are overgrown with a thin shell determined by the different growth conditions, enabling the fabrication of radial heterostructures.<sup>11–14</sup> Radial dopant profiles, for example, have been put forward as ideal geometry for photovoltaic and LED nanowire applications.<sup>15,16</sup> In this configuration the p-n-junction extends over the whole nanowire length, facilitating carrier injection and extraction. However, the successful application of nanowires will critically rely on the control and experimental verification of the

local free-carrier concentration,<sup>6,17–19</sup> which is still a challenging task.

Recently, it has been reported that the spatial distribution of impurity dopants incorporated by VLS and shell growth can be determined by using laser-pulsed atom probe microscopy (APM).<sup>18</sup> However, laser-pulsed APM is a destructive technique and due to surface and shielding effects<sup>20</sup> not all dopants necessarily have to be ionized, yielding a free-carrier concentration that may be reduced compared to the chemical dopant concentration. Garnett et al.<sup>19</sup> reported the radial free-carrier profile of single silicon nanowires by capacitance–voltage measurements, but this technique requires electrical contacts and does not provide nanoscale resolution in axial direction. Since for the deployment of the nanowires in optical and electronic devices the *local* conductivity is a critical parameter, nanoscale resolved free-carrier mapping is of utmost importance in order to tune and optimize the fabrication process. Consequently, different methods are explored in this direction, including electron holography microscopy,<sup>21</sup> Kelvin probe force microscopy<sup>22</sup> and scanning spreading resistance microscopy.<sup>23</sup> Here we report nanoscale mapping of free carriers in axially and radially modulation-doped InP nanowires (see Figure 1a) by scattering-type scanning near-field optical microscopy (s-SNOM). In s-SNOM,<sup>24</sup> an atomic force microscope (AFM) tip is illuminated by a focused infrared (IR) laser beam. Nanoscale free-carrier mapping is achieved by recording the amplitude and phase of light backscattered from the metalized AFM tip, simultaneously to the topography.<sup>25–27</sup>

\*To whom correspondence should be addressed. E-mail: r.hillenbrand@nanogune.eu.

Received for review: 01/15/2010

Published on Web: 03/19/2010

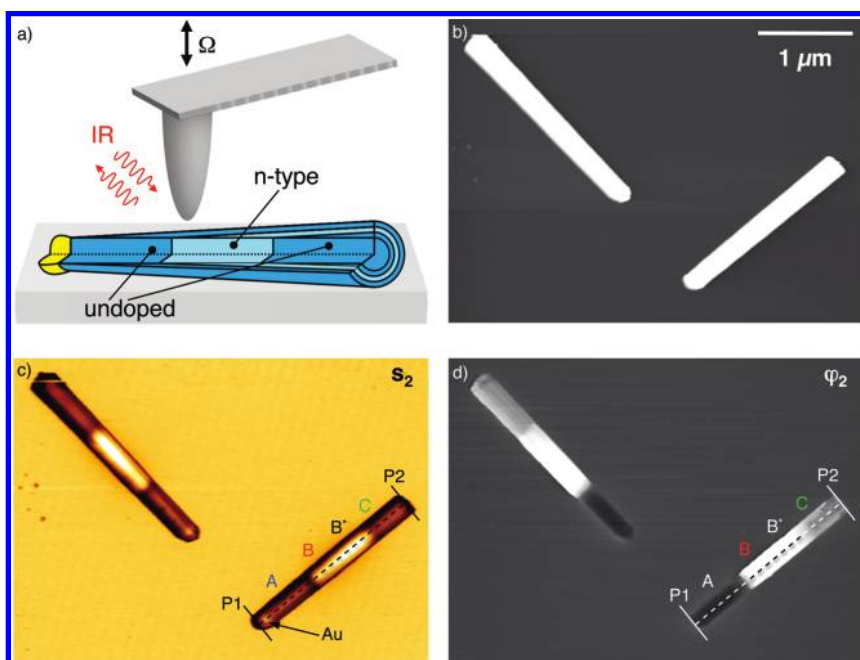


**FIGURE 1.** Infrared near-field mapping of modulation doped InP nanowires. (a) Schematic illustration of free-carrier profiling of modulation-doped semiconductor nanowires by infrared s-SNOM. (b–d) Topography and infrared amplitude  $s_2$  and phase  $\varphi_2$  images of two representative InP nanowires recorded at an IR laser frequency of  $893\text{ cm}^{-1}$  ( $11.2\text{ }\mu\text{m}$  wavelength). For s-SNOM measurements the InP nanowires are adsorbed on a flat silicon surface.

Near-field optical imaging was performed with our home-built infrared s-SNOM.<sup>24</sup> It is based on an AFM in which conventional Pt-coated Si-tips (apex radius  $\approx 20\text{ nm}$ ) are illuminated by a focused  $\text{CO}_2$  laser beam at frequencies between  $890$  and  $1100\text{ cm}^{-1}$  (Figure 1a). Nanoscale-resolved IR imaging is realized by recording the light backscattered from the tip. Operating the AFM in tapping mode, the tip is vertically vibrating with an amplitude of about  $20\text{--}30\text{ nm}$  at a frequency of  $\Omega \sim 300\text{ kHz}$ . Background-free near-field IR imaging is achieved by pseudoheterodyne interferometric detection of the backscattered light and subsequent demodulation of the detector signal at the  $n$ th harmonic of the tapping frequency,  $n\Omega$ .<sup>28</sup> In the present experiments, second harmonic demodulation ( $n = 2$ ) was employed, yielding amplitude  $s_2$  and phase  $\varphi_2$  images, simultaneously to topography.

InP wires comprising three different segments were prepared by growing vertically standing nanowires in the VLS growth mode on an InP surface.<sup>5</sup> For the s-SNOM measurements, the InP nanowires were transferred mechanically from the InP substrate onto a silicon wafer. The geometry of the nanowires is displayed in Figure 1a. First an undoped segment was grown followed by a highly sulfur (S) doped segment. The third, undoped, segment is grown with the same parameters as the first segment. In the following, we quantitatively determine the free-carrier concentration in the three different segments. (A) The undoped top segment terminated by the Au catalyst particle, (B) the middle segment containing a doped core coated by a doped inner shell, which shows a decrease of thickness along the

growth direction and an uniform undoped outer shell, and (C) the bottom segment where the undoped core is coated with a uniformly doped interior shell and an undoped outer shell. The thin shells in segments (B) and (C) arise from the slow radial growth that takes place simultaneously to the axial growth but at a lower growth rate.<sup>11–14</sup>

Figure 1b shows the topography of two InP wires and the simultaneously recorded IR amplitude  $s_2$  (Figure 1c) and phase  $\varphi_2$  images (Figure 1d) at a laser frequency of  $\omega = 893\text{ cm}^{-1}$ . While the topography image shows the uniform surface of the wires, the IR images clearly reveal the three different segments. Obviously, the IR amplitude and phase contrasts allow for distinguishing between the doped and undoped segments. Linescans (Figure 2a) showing the infrared amplitude and phase along the axis of the right wire also reveal a clear material contrast between the Au particle and the undoped InP segment. In agreement with former s-SNOM studies, the metal exhibits higher IR amplitudes than the undoped semiconductor material.<sup>25,26</sup> From the sharp change of the amplitude signal at the Au/InP interface wire we can estimate a spatial resolution of about  $25\text{ nm}$ .

Before analyzing the measured IR contrast along the InP wires, we illustrate the capability of free-carrier mapping in doped nanowires by calculating amplitude and phase of the tip-scattered radiation by using the finite-dipole model.<sup>29</sup> In this model, amplitude and phase signals are derived from the near-field interaction between the probing tip and a bulk sample characterized by its dielectric function  $\epsilon_{\text{InP}}$ . In our calculations, we use literature values for the dielectric function of undoped InP.<sup>30</sup> The presence of free carriers is taken

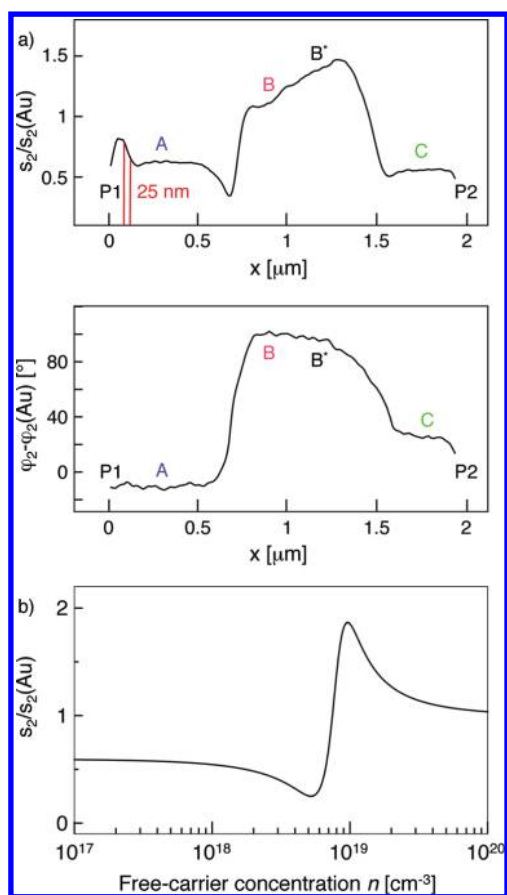


FIGURE 2. (a) IR amplitude  $s_2$  and phase  $\varphi_2$  along the axis of the right nanowire in Figure 1c, extracted between the two positions marked P1 and P2. The letters A–C mark the positions of the infrared near-field spectra shown in Figures 4 and 5. (b) Calculated s-SNOM amplitude  $s_2$  of an InP sample with an increasing free-carrier concentration from  $10^{17}$  to  $10^{20}$  carriers/cm $^{-3}$  at the fixed IR frequency of  $893\text{ cm}^{-1}$  (corresponding to  $11.19\text{ }\mu\text{m}$  wavelength). The calculation was carried out employing the finite-dipole model $^{29}$  and normalized to the s-SNOM signal of an Au sample.

into account by a Drude-term, yielding a dielectric function of InP given by

$$\epsilon_{\text{InP}}(\omega) = \epsilon_{\infty} \left( 1 - \frac{\omega_p^2}{\omega^2 + i\omega\gamma} \right)$$

where  $\omega_p$  is the plasma frequency, which depends on the free-carrier concentration  $n$  as  $\omega_p^2 \sim n$ , whereas the damping  $\gamma \sim 1/\mu$  inversely scales with the concentration-dependent carrier mobility  $\mu(n)$ . For the carrier mobility, we first assume in the model values for bulk material taken from ref 31.

We first calculate the IR amplitude  $s_2$  as a function of the free-carrier concentration  $n$  for the fixed frequency  $\omega = 893\text{ cm}^{-1}$ , which was employed for recording the images shown in Figure 1. Figure 2b shows that with increasing  $n$  the calculated amplitude first exhibits a minimum at around  $n$

$\approx 5 \times 10^{18}\text{ cm}^{-3}$ , followed by a maximum at about  $n \approx 10^{19}\text{ cm}^{-3}$ . This resonance behavior $^{25}$  arises from the near-field interaction between the probing tip and the free carriers (plasmons) in a highly doped semiconductor sample. $^{25,32}$  As for any resonance, the amplitude maximum is accompanied by a strong phase change. Indeed, this resonance behavior is clearly seen in the experimental line-plot shown in Figure 2a. The significant amplitude minimum (around  $x = 0.7\text{ }\mu\text{m}$ ) directly reveals the existence of a free-carrier gradient between the undoped (A) and doped (B) segments, extending more than  $200\text{ nm}$  along the nanowire axis, as we can estimate by comparing Figure 2a,b.

Intriguingly, in Figures 1d and 2a we also observe a phase contrast between the undoped top segment (A) and the bottom segment (C), the latter consisting of an undoped core, but with an interior doped shell. The thickness of the doped shell can be estimated to be about  $10\text{ nm}$  and is covered by an approximately  $10\text{ nm}$  thick undoped shell (both thicknesses can be determined from the topography of the wire, showing a linear increase of the diameter from  $100$  to  $140\text{ nm}$ ). The successful detection of the doped subsurface shell has two important implications. It demonstrates that infrared near-field microscopy enables noninvasive and nanoscale resolved free-carrier mapping inside a single nanowire heterostructure. Further, it provides direct experimental evidence that doping introduced during radial nanowire growth yields a large free-carrier concentration, that is, local conductivity, which has important consequences for future device designs.

For a better understanding of the near-field IR free-carrier contrast, we calculate the infrared amplitude  $s_2$  and phase  $\varphi_2$  signals as a function of the illumination frequency  $\omega$  (Figure 3). We observe a distinct spectral behavior with a resonance shifting to higher frequencies when the free-carrier concentration  $n$  increases. This resonance, already seen in Figure 2b, can be explained by a plasmon-resonant near-field interaction $^{25,26}$  between the tip and the doped InP surface, which typically occurs near the plasma frequency  $\omega_p$ . The infrared near-field signal thus provides a significant and highly sensitive spectral signature from which the local free-carrier concentration can be determined, as we will show in the following.

To quantify the free-carrier concentration in the doped InP nanowire segment, we perform near-field spectroscopic mapping of the right nanowire in Figure 1 in the spectral range  $\omega = 890\text{--}1100\text{ cm}^{-1}$ . Local amplitude and phase spectra taken at the top (A), middle (B), and bottom (C) segments are shown in Figure 4a. The spectra of the undoped top segment (position A in Figure 1, blue symbols) do not exhibit any spectral signature in both amplitude and phase. The doped core (position B in Figure 1, red symbols), in contrast, reveals a significant spectral signature. With increasing frequency we find a strong signal decrease in both the amplitude and phase. Applying the finite-dipole model, $^{29}$  we can fit the experimental data. The free-carrier concentra-

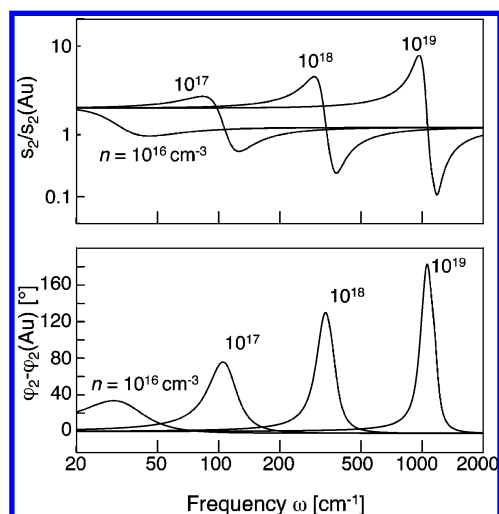


FIGURE 3. Calculation of s-SNOM amplitude and phase spectra,  $s_2$  and  $\varphi_2$ , for InP samples of different free-carrier concentration  $n$  ranging from  $10^{16}$  to  $10^{19}$   $\text{cm}^{-3}$ . The calculations were carried out employing the finite-dipole model<sup>29</sup> and normalized to the s-SNOM signal obtained for an Au sample. We note that for illustrating the plasmonic s-SNOM response in Figure 2 we neglect the contribution of optical phonons in InP at around  $350$   $\text{cm}^{-1}$ .

tion  $n$  and free-carrier mobility  $\mu$  are used as fit parameters. Because of the flat spectral characteristics for the undoped segment (A) we can only estimate an upper limit for the doping concentration in this segment. We find a good agreement between experiment and calculation for  $n < 10^{18}$   $\text{cm}^{-3}$  (solid blue line). For the doped segment at position B, we obtain good agreement in both amplitude and phase for  $n = 7.6 \times 10^{18}$   $\text{cm}^{-3}$  and a mobility that is reduced by a factor of 0.45 with respect to the literature value for bulk InP (solid red line).<sup>30,31</sup> Possible reasons for the reduced mobility could be the wire geometry or the high-frequency (IR) measurement. For different bulk semiconductors, it has been reported that the mobility at IR frequencies can be significantly reduced compared to the DC mobility.<sup>33</sup> Furthermore, radial variations in the free-carrier contribution, often observed in doped semiconductor nanowires,<sup>18,19</sup> could broaden the near-field resonance. Thus, fitting the resonance would yield an averaged free-carrier concentration of the local volume probed by the near field of the tip and a reduced mobility. A promising pathway to tackle this issue in the future could be the development of near-field tomography, which could allow for depth-resolved near-field mapping of local material properties.<sup>34,35</sup> Nevertheless, the already demonstrated capability to retrieve free-carrier concentration and mobility with nanoscale spatial resolution promises s-SNOM to become a highly interesting tool not only for nanowire research.

We next study the IR near-field spectrum of the doped interior shell of the nanowires' bottom segment (Figure 4a, spectrum C displayed by green symbols). Interestingly, we find a clear signature in the phase spectrum. While both the spectral amplitude and phase contrasts are significantly reduced, the spectral feature appears in the same frequency

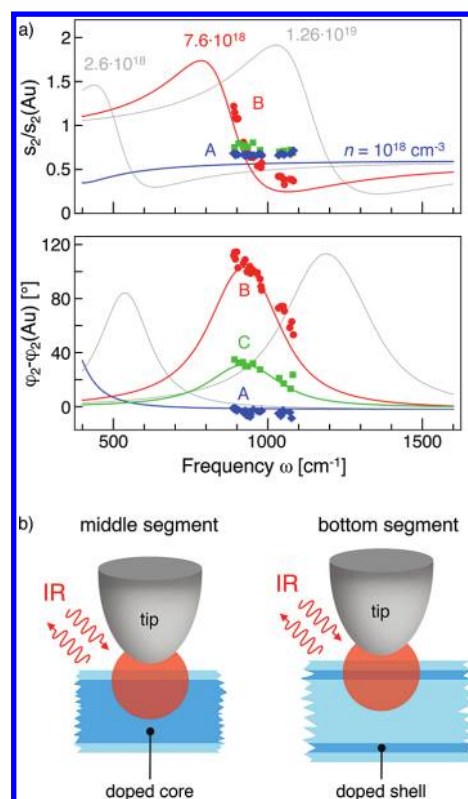
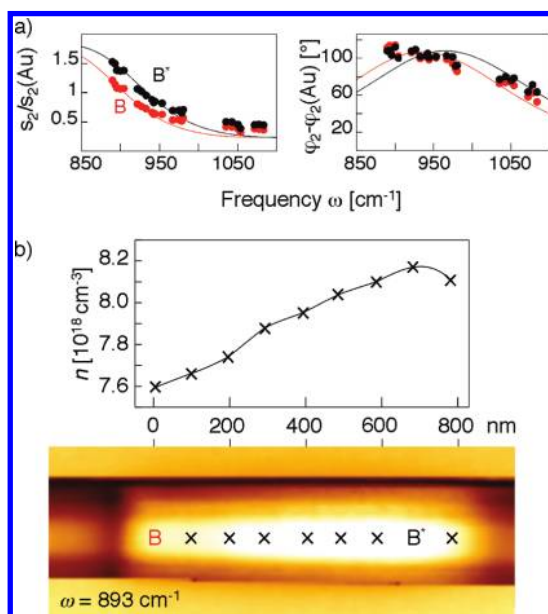


FIGURE 4. Local infrared near-field spectra of a single InP nanowire. (a) The red and blue curves show amplitude and phase spectra taken at positions A (undoped InP) and B (doped InP core) marked in Figure 1b. The green curve C was taken at the center of the bottom segment (doped InP shell) of an InP nanowire of the same nanowire sample. Both experimental (symbols) and theoretical (solid lines) amplitude  $s_2$  and phase  $\varphi_2$  spectra were normalized to the signal obtained on the Au particle. Numbers indicate the free-carrier concentration  $n$  used for the calculations. The gray curves show calculated spectra with increased and decreased free-carrier concentration ( $\pm 5 \times 10^{18}$   $\text{cm}^{-3}$ ) illustrating that changes in the range of 50% would yield large spectral shifts of several  $100$   $\text{cm}^{-1}$ . (b) Schematic drawing of the highly doped middle segment and the highly doped subsurface shell, respectively.

range as for the doped core (middle segment, position B). We illustrate this finding by multiplying the phase spectrum B of the doped core with a factor of 0.5. The good agreement with the experimental phase spectrum C confirms the absence of a pronounced spectral shift between spectra B (doped core) and C (doped shell). Because the spectral position of the phase slope is determined by the free-carrier concentration  $n$  (see Figure 2 and gray curves in Figure 4a), we can conclude that the effective free-carrier concentration is similarly high as in the doped core. Considering that the dopant concentration in the shell can be expected to be higher than inside the core,<sup>18</sup> this is an interesting observation. We explain it by the fact that the doped shell is clamped between the undoped core and the undoped outer shell. Because of the strong difference in concentration, free carriers diffuse toward the undoped regions. Therefore, the observed free-carrier concentration is lower than the chemically built-in dopant concentration. We note that the weaker spectral contrast in both amplitude and phase can be



**FIGURE 5.** Sensitivity of s-SNOM demonstrated on the highly doped middle segment. (a) Near-field spectra of the central segment at positions B and B\*, revealing a slight difference in free-carrier concentration amounting to about  $\Delta n = 0.5 \times 10^{18} \text{ cm}^{-3}$ . (b) Measured free-carrier concentration along the central nanowire segment, shown together with a high-resolution infrared image at  $893 \text{ cm}^{-1}$ . The data-points in Figure 5 have been calculated by finding the best agreement for amplitude and phase between the finite-dipole model calculation and the measured near-field spectra at each position.

explained by the reduced amount of doped material that is probed by the IR near-field at the tip apex (Figure 4b). The reduced spectral contrast is a typical observation when the near-field contrast of a thin layer is compared with a bulk sample of the same material.<sup>56</sup>

We now study in more detail the amplitude signal  $s_2$  on the central segment, which clearly increases along the axial direction (Figure 2). Comparing the spectra taken at position B and B\* (Figure 5a), we find a slight shift of spectrum B\* toward higher frequencies. This corresponds to an increase of the free-carrier concentration of about  $\Delta n = 0.5 \times 10^{18} \text{ cm}^{-3}$  (6.6%). Evaluating local near-field spectra along the nanowire axis, we find a linearly increasing free-carrier concentration (Figure 5b). At first, this data evaluation highlights the powerful combination of high sensitivity and nanoscale spatial resolution provided by IR spectroscopic s-SNOM. Furthermore, it indicates that the local free-carrier concentration on the doped segment slightly increases with increasing thickness of the inner doped shell. This could be explained by the higher dopant concentration in the shell compared to the core,<sup>18</sup> yielding a higher number of dopants with increasing shell thickness.

Finally, we demonstrate the intriguing sensitivity of s-SNOM to local free-carriers in even very thin nanowires. In Figure 6, we show modulation-doped InP nanowires with diameters as small as 20 nm, which were grown with the same growth-protocol as the 100 nm wires presented in

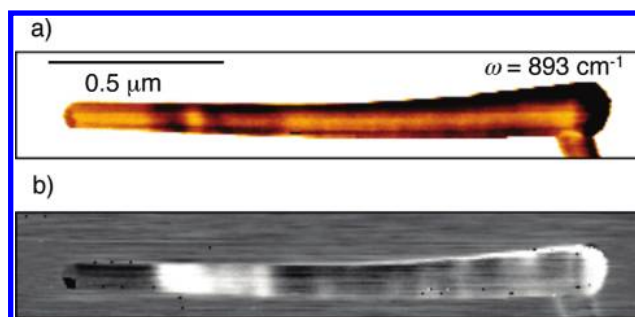


**FIGURE 6.** Infrared near-field images of modulation doped InP nanowires with a thickness of 20 nm. (a) Amplitude and (b) phase images recorded at a frequency of  $895 \text{ cm}^{-1}$  ( $11.17 \mu\text{m}$  wavelength) of a representative nanowire, grown with the same procedure as the 100 nm InP wires.

Figure 1. The IR images clearly reveal the doped segment. In contrast to the 100 nm wires, however, the doped segment is substantially shorter, owing to reduced axial growth speed in thin wires.<sup>37</sup> Furthermore, the doped segment exhibits strong signal variations in both IR amplitude and phase, which indicates a strongly inhomogeneous free-carrier distribution. We assign this finding to an increased defect density in thin wires<sup>38,39</sup> but further systematic studies are certainly needed for an in-depth understanding of this observation. We expect that future combined TEM and s-SNOM studies will provide deeper insights into the interplay between structural and electronic properties in doped semiconductor nanowires.

In conclusion, we demonstrated the application of infrared near-field nanoscopy for highly sensitive and nanoscale resolved mapping of free carriers in doped semiconductor nanowires. Provided radial carrier variations can be excluded, the method allows for the measurement of local carrier concentration and mobility. Sensitivity to lower free-carrier concentrations can be achieved by spectral extension<sup>40</sup> of s-SNOM to terahertz frequencies.<sup>26</sup> In case of three-dimensional free-carrier distributions, that is, both axial and radial variations of the carrier density, future quantitative measurements will require systematic studies and improved modeling of subsurface near-field mapping<sup>41</sup> and depth resolution in s-SNOM. The implementation of near-field optical tomography, recently predicted to provide three-dimensional information about the local dielectric properties,<sup>35</sup> could open the door to noninvasive mapping of the three-dimensional distribution of both the free-carrier concentration and mobility not only in complex nanowire heterostructures but also in single nanoparticles and nanodevices.

**Acknowledgment.** The authors thank J. Aizpurua and A. García Etxarri for stimulating discussions, and G. Immink for nanowire growth. This work was supported by the National Plan Project MAT2009-08398 from the Spanish Ministerio de Ciencia e Innovacion and the EU program NODE (015783) and is part of the research program of the “Stichting voor Fundamenteel Onderzoek der Materie (FOM)”, which is

financially supported by the “Nederlandse organisatie voor Wetenschappelijk Onderzoek (NWO)”. It is also part of an industrial partnership program between Philips and FOM.

## REFERENCES AND NOTES

- (1) Huang, M. H.; Mao, S.; Feick, H.; Yan, H.; Wu, Y.; Kind, H.; Weber, E.; Russo, R.; Yang, P. *Science* **2001**, *292* (5523), 1897.
- (2) Duan, X. F.; Huang, Y.; Agarwal, R.; Lieber, C. M. *Nature* **2003**, *421* (6920), 241.
- (3) Thelander, C.; Nilsson, H. A.; Jensen, L. E.; Samuelson, L. *Nano Lett.* **2005**, *5* (4), 635.
- (4) Goodey, A. P.; Eichfeld, S. M.; Lew, K. K.; Redwing, J. M.; Mallouk, T. E. *J. Am. Chem. Soc.* **2007**, *129*, 12344.
- (5) Minot, E. D.; Kelkensberg, F.; van Kouwen, M.; van Dam, J. A.; Kouwenhoven, L. P.; Zwiller, V.; Borgström, M. T.; Wunnicke, O.; Verheijen, M. A.; Bakkers, E. P. A. M. *Nano Lett.* **2007**, *7* (2), 367.
- (6) Colli, A.; Fasoli, A.; Ronning, C.; Pisana, S.; Piscanec, S.; Ferrari, A. *Nano Lett.* **2008**, *8* (8), 2188.
- (7) Björk, M. T.; Ohlsson, B. J.; Sass, T.; Persson, A. I.; Thelander, C.; Magnusson, M. H.; Deppert, K.; Wallenberg, L. R.; Samuelson, L. *Nano Lett.* **2002**, *2* (2), 87.
- (8) van Weert, M. H. M.; Helman, A.; van den Einden, W.; Algra, R. E.; Verheijen, M. A.; Borgström, M. T.; Immink, G.; Kelly, J. J.; Kouwenhoven, L. P.; Bakkers, E. J. *Am. Chem. Soc.* **2009**, *131* (13), 4578.
- (9) Van Dam, J. A.; Nazarov, Y. V.; Bakkers, E.; De Franceschi, S.; Kouwenhoven, L. P. *Nature* **2006**, *442* (7103), 667.
- (10) Verheijen, M. A.; Algra, R. E.; Borgström, M. T.; Immink, G.; Sourty, E.; van Enckevort, W. J. P.; Vlieg, E.; Bakkers, E. *Nano Lett.* **2007**, *7* (10), 3051.
- (11) Lauhon, L. J.; Gudiksen, M. S.; Wang, C. L.; Lieber, C. M. *Nature* **2002**, *420* (6911), 57.
- (12) Sköld, N.; Karlsson, L. S.; Larsson, M. W.; Pistol, M.-E.; Seifert, W.; Trägårdh, J.; Samuelson, L. *Nano Lett.* **2005**, *5* (10), 1943.
- (13) Li, H. Y.; Wunnicke, O.; Borgstrom, M. T.; Immink, W. G. G.; van Weert, M. H. M.; Verheijen, M. A.; Bakkers, E. P. A. M. *Nano Lett.* **2007**, *7* (5), 1144.
- (14) Verheijen, M. A.; Immink, G.; de Smet, T.; Borgström, M. T.; Bakkers, E. P. A. M. *J. Am. Chem. Soc.* **2006**, *128* (4), 1353.
- (15) Colombo, C.; Heiß, M.; Grätzel, M.; Fontcuberta i Morral, A. *Appl. Phys. Lett.* **2009**, *94* (17), 173108–3.
- (16) Kelzenberg, M. D.; Turner-Evans, D. B.; Kayes, B. M.; Filler, M. A.; Putnam, M. C.; Lewis, N. S.; Atwater, H. A. *Nano Lett.* **2008**, *8* (2), 710.
- (17) Pearton, S. J.; Norton, D. P.; Ren, F. *Small* **2007**, *3* (7), 1144.
- (18) Perea, D. E.; Hemesath, E. R.; Schwalbach, E. J.; Lensch-Falk, J. L.; Voorhees, P. W.; Lauhon, L. J. *Nat. Nanotechnol.* **2009**, *4* (5), 315.
- (19) Garnett, E. C.; Tseng, Y.-C.; Khanal, D. R.; Wu, J.; Bokor, J.; Yang, P. *Nat. Nanotechnol.* **2009**, *4* (5), 311.
- (20) Diarra, M.; Niquet, Y. M.; Delerue, C.; Allan, G. *Phys. Rev. B.* **2007**, *75* (4), 045301.
- (21) den Hertog, M. I.; Schmid, H.; Cooper, D.; Rouviere, J. L.; Björk, M. T.; Riel, H.; Rivallin, P.; Karg, S.; Riess, W. *Nano Lett.* **2009**, *9* (11), 3837–3843.
- (22) Vinaji, S.; Lochthofen, A.; Mertin, W.; Regolin, I.; Gutsche, C.; Prost, W.; Tegude, F. J.; Bacher, G. *Nanotechnology* **2009**, *20* (38), 385702.
- (23) Ou, X.; Kanungo, P. D.; Kögler, R.; Werner, P.; Gösele, U.; Skorupa, W.; Wang, X. *Nano Lett.* **2010**, *10*, 171–175.
- (24) Keilmann, F.; Hillenbrand, R. *Philos. Trans. R. Soc., London, Ser. A* **2004**, *362* (1817), 787.
- (25) Huber, A. J.; Kazantsev, D.; Keilmann, F.; Wittborn, J.; Hillenbrand, R. *Adv. Mater.* **2007**, *19* (17), 2209.
- (26) Huber, A. J.; Keilmann, F.; Wittborn, J.; Aizpurua, J.; Hillenbrand, R. *Nano Lett.* **2008**, *8* (11), 3766.
- (27) Qazilbash, M. M.; Brehm, M.; Chae, B.-G.; Ho, P.-C.; Andreev, G. O.; Kim, B.-J.; Yun, S. J.; Balatsky, A. V.; Maple, M. B.; Keilmann, F.; Kim, H.-T.; Basov, D. N. *Science* **2007**, *318* (5857), 1750–1753.
- (28) Ocelic, N.; Huber, A.; Hillenbrand, R. *Appl. Phys. Lett.* **2006**, *89* (10), 3.
- (29) Cvitkovic, A.; Ocelic, N.; Hillenbrand, R. *Opt. Express* **2007**, *15* (14), 8550.
- (30) Ibáñez, J.; Cuscó, R.; Artús, L. *Phys. Status Solidi B* **2001**, *223* (3), 715–722.
- (31) Sotoodeh, M.; Khalid, A. H.; Rezazadeh, A. A. *J. Appl. Phys.* **2000**, *87* (6), 2890.
- (32) Knoll, B.; Keilmann, F. *Appl. Phys. Lett.* **2000**, *77* (24), 3980–3982.
- (33) Jeon, T. I.; Grischkowsky, D. *Phys. Rev. Lett.* **1997**, *78* (6), 1106.
- (34) Carney, P. S.; Schotland, J. C. *Appl. Phys. Lett.* **2000**, *77* (18), 2798–2800.
- (35) Sun, J.; Schotland, J. C.; Hillenbrand, R.; Carney, P. S. *Appl. Phys. Lett.* **2009**, *95* (12), 121108–3.
- (36) Aizpurua, J.; Taubner, T.; García de Abajo, F. J.; Brehm, M.; Hillenbrand, R. *Opt. Express* **2008**, *16* (3), 1529.
- (37) Borgström, M. T.; Immink, G.; Ketelaars, B.; Algra, R.; Bakkers, E. *Nat. Nanotechnol.* **2007**, *2*, 541–544.
- (38) Algra, R. E.; Verheijen, M. A.; Borgström, M. T.; Feiner, L.-F.; Immink, G.; van Enckevort, W. J. P.; Vlieg, E.; Bakkers, E. P. A. M. *Nature* **2008**, *456* (7220), 369–372.
- (39) Caroff, P.; Dick, K. A.; Johansson, J.; Messing, M. E.; Deppert, K.; Samuelson, L. *Nat. Nanotechnol.* **2009**, *4* (1), 50–55.
- (40) Amarie, S.; Ganz, T.; Keilmann, F. *Opt. Express* **2009**, *17* (24), 21794–21801.
- (41) Taubner, T.; Keilmann, F.; Hillenbrand, R. *Opt. Express* **2005**, *13* (22), 8893–8899.